Recent Progress toward High Efficiency Bulk Heterojunction Solar Cells

Wanli Ma[1], Cuiying Yang[1], Xiong Gong[1], Jin Young Kim[1,2], Sun Hee Kim[2], Hyun-Ho Lee[2], Kwanghee Lee[1,2], and Alan J. Heeger[1]

[1]Center for Polymers and Organic Solids, University of California

Santa Barbara, California 93106-5090, USA

[2]Department of Physics, Pusan National University, Busan 609-735, Korea

Abstract

Polymer solar cells with power conversion efficiencies approaching 5% are demonstrated. These devices exhibit remarkable thermal stability. We attribute the improved performance to changes in the bulk heterojunction material induced by thermal annealing. The improved nanoscale morphology, the increased crystallinity of the semiconducting polymer, and the improved contact to the electron collecting electrode facilitate charge generation, charge transport to, and charge collection at the electrodes. Solar cells with a TiO_x layer (deposited by a sol-gel process) between the active layer and the electron collecting aluminum electrode exhibit approximately 50% enhancement in power conversion efficiency compared to similar devices without the optical spacer. The TiO_x layer increases the efficiency by modifying the spatial distribution of the light intensity inside the device, thereby creating more photogenerated charge carriers in the bulk heterojunction layer.

Introduction

Solar cell technology based on conjugated polymer-fullerene composites continues

to be of interest as a potential source of renewable energy. [1-5] In particular, because of the light weight, the mechanical flexibility, and the potential for low-cost production of electronic devices fabricated from semiconducting polymers, high efficiency polymer solar cells could have major impact on energy needs. Although encouraging progress has been made in recent years with 3-4% power conversion efficiencies under AM1.5 (AM=air mass) illumination, [6] this efficiency is not yet sufficient for large scale implementation. Moreover, concerns about instability at elevated temperatures have hindered the path toward commercialization. The need to improve the device efficiency and thermal stability requires state-of-the-art fabrication and treatment under more rigorously defined conditions.

The device performance of a photovoltaic cell is characterized by the short-circuit current (I_{sc}), open-circuit voltage (V_{oc}), and fill factor (FF). Higher values of these three parameters yield larger light-to-electricity power conversion efficiency (η_e);

$$\eta_e = I_{sc} V_{oc} FF. \qquad (1)$$

Thus, the device efficiency can be enhanced by implementing fabrication procedures that influence I_{sc} and FF (for a specific donor/ acceptor system, V_{oc} is determined by the energy level difference between the component materials of the composite [7,8]).

Based upon the equivalent circuit of a photovoltaic cell,[9] the I-V characteristics can be described by the following equation: [10]

$$I = I_0 \times [\exp(e\frac{U - IR_S}{nkT}) - 1] + \frac{U - IR_S}{R_{SH}} - I_{PH} \qquad (2)$$

where I_0 is the dark current, e is the electron charge, n is the diode ideality factor, U is the applied voltage, R_S is the series resistance, R_{SH} is the shunt resistance, and I_{PH} is the photocurrent. Thus, to obtain high short circuit currents, I_{SC} (U = 0 volts), solar cell devices must have small R_S and large R_{SH}. The fill factor can be written as:

$$FF = \frac{V_{MPP} \times I_{MPP}}{V_{OC} \times I_{SC}} \qquad (3)$$

where the subscript MPP denotes the maximum power point. Thus, a large FF requires that the photocurrent rise abruptly as U approaches V_{OC} (i.e. to obtain the maximum of the $V_{MPP} \times I_{MPP}$ product). This optimum condition can only be met when the photo-generated carriers are extracted without significant loss from recombination. Therefore, the fill factor is limited by the carrier drift length, L_d

$$L_d = \mu \, . \, \tau \, . \, E$$

where μ is the carrier mobility, τ is the carrier recombination lifetime, and E is the electric field; L_d must be longer than the active layer thickness to prevent significant loss by recombination.[11,12] Hence a high mobility or thin film is necessary for efficient charge carrier extraction.

One approach toward improving both I_{sc} and FF is through postproduction heat treatment. Recent studies have demonstrated improved power conversion efficiencies after thermally annealing polymer-fullerene composite solar cells at elevated temperatures (50-130^{o}C).[6,13-16] In these earlier studies, the best results ($\eta_e \approx 3.5\%$) were obtained after postproduction thermal annealing at 75^{o}C for 5 minutes. [6]

By applying the specific device fabrication conditions and postproduction annealing at 150^{o}C, bulk heterojunction solar cells using poly(3-hexylthiophene) (P3HT) as the electron donor and [6,6]-phenyl-C_{61}butyric acid methyl ester (PCBM) as the electron acceptor can be demonstrated with 5% power conversion efficiency under AM1.5 illumination at 80 mW/cm^{-2} (device structure ITO/PEDOT/P3HT:PCBM/Al).

High Temperature Annealing: Results and Discussion

Figure 1 shows the current density vs voltage (I-V) characteristics under AM1.5 illumination from a calibrated solar simulator with an intensity of 80 mW/cm^2. The device without heat treatment shows poor performance with V_{oc} = 0.6 V, I_{sc} = 3.83 mA/cm^2, and FF = 30%. The power conversion efficiency (η_e) for this device is therefore only η_e = 0.82%. After thermal annealing at 70 ^{o}C for 30 minutes, I_{sc} and FF both increase such that η_e = 3.2%. This value is comparable to the previous report of η_e = 3.5% obtained after annealing for 5 minutes at 75 ^{o}C. [6] After annealing at 150^{o}C for 30 minutes, the device exhibits more pronounced improvement with I_{sc} = 9.5 mA/cm^2 and FF = 68% [see Fig. 1], while V_{oc} remains nearly constant at 0.63 V as expected. The corresponding power conversion efficiency is η_e = 5%, the highest value reported to date for a polymer based photovoltaic cell.

The increase in I_{sc} (and the improved FF) implies a significant decrease in the series resistance (see eqn. 2). From numerical analysis of eqn. 2, we find that the series

resistance decreases from an initial value of $R_s = 113\,\Omega$ to $R_s = 7.9\,\Omega$ after annealing at 150°C.

By utilizing the optimized fabrication procedure, our devices exhibited both outstanding efficiency and extraordinary thermal stability. Over 100 individual samples were measured with efficiencies ranging between 4.8% and 5.1%.

Fig 2 summarizes the results of a comprehensive study of FF, I_{SC} and η_e as a function of the annealing temperature. As shown in the inset of Fig. 2a, the efficiency increases with the annealing temperature. Note that a significant increase is observed at ~ 50°C; i.e. near the glass transition temperature of P3HT (consistent with our differential scanning calorimetry measurements). The optimum annealing temperature is 150°C. The effect of annealing at 150°C for different periods of time is shown in Fig. 2b; the device efficiency tends toward saturation after annealing for 30 minutes at 150°C.

We observed stable solar cell performance even after annealing for hours at 150°C, as shown in Fig. 2b. This remarkable stability indicates the formation of thermally stable nano-scale interpenetrating donor-acceptor networks. Devices annealed at high temperature during fabrication are expected to be even more stable under ambient conditions.

Previous publications on the effects of thermal annealing reported a sudden drop in efficiency after annealing for only a few seconds at 130°C or a few minutes at 75°C.

[6,13] The origin of this instability was degradation of the morphology resulting from the formation of large PCBM aggregates.[17] Other more recent work has also focused on the opportunity to improve device performance through high temperature annealing.[18-20] By using chlorobenzene as the solvent and reducing the P3HT/PCBM ratio and concentration, the overgrowth of the PCBM aggregates has been suppressed. This nano-scale control of the morphology of the D-A interpenetrating networks results in optimized and stable phase separation for efficient charge separation and transport and thereby leads to thermally stable, high efficiency solar cells.

From Eqns. 2 and 3, the larger values for I_{sc} and FF imply lower series resistance and higher carrier mobility (as noted above, the series resistance decreases from an initial value of $R_s = 113\,\Omega$ to $R_s = 7.9\,\Omega$ after annealing at 150°C). Thus, the increased efficiency results from two effects: higher nanoscale crystallinity and improved microstructure with demixing between the two components in the bulk heteorjunction films after thermal annealing.

Transmission electron microscopy (TEM) images of the P3HT:PCBM films before and after thermal annealing, are shown in Fig. 3. Without any heat treatment, the interpenetrating networks are not well developed, and the donor/acceptor (D/A) domains are difficult to distinguish. After thermal annealing for 30 minutes and two hours, respectively, the morphology of the interpenetrating D/A networks becomes clearer and easily visible with a typical feature size of ~10 nm. This characteristic

length scale is consistent with observations reported in previous studies.[21,22] The changes in morphology result in a large interfacial area for efficient charge generation.

The high temperature anneal also improves the crystallinity within the phase separated networks and thereby facilitates charge transport to the electrodes. The increased crystallinity of P3HT can be seen clearly in the X-ray diffraction (XRD) results shown in Fig. 4(a). Increased intensity is observed in the peak at $2\theta \approx 5^{o}$ (corresponding to the interchain spacing in P3HT associated with the interdigitated alkyl chains) and in the peak at $2\theta \approx 23^{o}$ (corresponding to the interchain spacing in P3HT associated with face to face packing of the thiophene rings).[23] The data in Fig. 4a were obtained from a drop-cast film of P3HT:PCBM. X-ray diffraction data obtained from an actual completed device are shown in Fig. 4b. Again, the increased crystallinity is evident from the peak at $2\theta \approx 5^{o}$.

Fig. 5 demonstrates the importance of the Al interface in the annealing process that leads to high efficiency. While the devices annealed prior to Al deposition show modest improvement (from 3.0% to 3.5%) and significant degradation at temperatures above 100^{o}C, the devices annealed after Al deposition exhibit enhanced efficiencies and better thermal stability, as demonstrated in detail in Fig. 2.

New Architecture for Bulk Heterojunction Solar Cells: The Concept

Polymer-based photovoltaic cells are thin film devices fabricated in the metal-insulator-metal configuration sketched in Fig. 6A. The absorbing and charge separating bulk heterojunction layer with thickness of approximately 100 nm is sandwiched between two charge selective electrodes; a transparent bilayer electrode comprising poly(3,4-ethylenedioxylenethiophene)-polystylene sulfonic acid (PEDOT:PSS) on indium-tin-oxide (ITO) glass for collecting the holes and a lower work-function metal (here, Al) for collecting the electrons. The work-function difference between the two electrodes provides a built-in potential that breaks the symmetry thereby providing a driving force for the photo-generated electrons and holes toward their respective electrodes.

Because of optical interference between the incident (from the ITO side) and back-reflected light, the intensity of the light is zero at the metallic (Al) electrode (*27-29*). Thus, as sketched in Fig. 6A, a relatively large fraction of the active layer is in a dead-zone in which the photogeneration of carriers is significantly reduced. Moreover, this effect causes more electron-hole pairs to be produced near the ITO/PEDOT:PSS electrode, a distribution which is known to reduce the photovoltaic conversion efficiency (*29,30*). This 'optical interference effect' is especially important for thin film structures where layer thicknesses are comparable to the absorption depth and the wavelength of the incident light, as is the case for photovoltaic cells fabricated from semiconducting polymers.

In order to overcome these problems, one might simply increase the thickness of the active layer to absorb more light. Because of the low mobility of the charge carriers in the polymer/C_{60} composites, however, the increased internal resistance of thicker films will inevitably lead to a reduced fill factor.

An alternative approach is to change the device architecture with the goal of spatially redistributing the light intensity inside the device by introducing an optical spacer between the active layer and the Al electrode as sketched in Fig. 6A. Although this revised architecture would appear to solve the problem, the prerequisites for an ideal optical spacer limit the choice of materials: The layer must be a good acceptor and an electron transport material with a conduction band edge lower in energy than that of the lowest unoccupied molecular orbital (LUMO) of C_{60}, the LUMO must be above (or close to) the Fermi energy of the collecting metal electrode, and it must be transparent to light with wavelengths within the solar spectrum.

Titanium dioxide (TiO_2) is a promising candidate as an electron acceptor and transport material. Typically, however, crystalline TiO_2 is used, either in the anatase phase or the rutile phase, both of which require treatment at temperatures ($T > 450^{\circ}C$) that are inconsistent with the device architecture shown in Fig. 6; the polymer/C_{60} composite cannot survive such high temperatures. We have used a solution-based sol-gel process to fabricate a titanium oxide (TiO_x) layer on top of the polymer-fullerene active layer (Fig. 6B). By introducing the TiO_x optical spacer, we

demonstrate polymer photovoltaic cells with power conversion efficiencies that are increased by approximately 50% compared to similar devices fabricated without the optical spacer.

The Optical Spacer

Dense TiO_x films were prepared using a TiO_x precursor solution, as described in detail elsewhere. The precursor solution was spin-cast in air on top of the polymer-fullerene composite layer. Subsequently, during one hour in air at room temperature, the precursor converts to TiO_x by hydrolysis. The sample was then heated at 150˚C for 10 minutes inside a glove box filled with nitrogen. The resulting TiO_x films are transparent and smooth with surface features smaller than few nm.

Scanning Electron Microscope (SEM) and separate Photon Correlation (Light Scattering) Spectroscopy measurements confirm that the average size of the TiO_x particles in the films is about 6 nm. However, since the layer was treated at 150˚C, the film is amorphous as confirmed by X-ray diffraction (XRD). The typical XRD peaks of the anatase crystalline form appear only after sintering the spin-cast films at 500˚C for 2 hours. Analysis by X-ray Photoelectron Spectroscopy (XPS) reveals an oxygen deficiency at the surface of the thin film samples with Ti : O ratio as 42.13% : 56.38%; hence we designate the composition as TiO_x.

In spite of the amorphous nature of the TiO_x layer, the physical properties are

excellent. The absorption spectrum of the film shows a well-defined absorption edge at $E_g \approx 3.7$ eV. Although this value is somewhat higher than that of the bulk anatase samples ($E_g \approx 3.2$ eV), the value is consistent with the calculation of the modified particle in a sphere model for the size dependence of semiconductor band gaps (*31*). Using optical absorption and Cyclic Voltammetry (CV) data, the energies of the bottom of the conduction band (LUMO) and the top of the valence band (HOMO) of the TiO_x material were determined; see Fig. 7. This energy level diagram demonstrates that the TiO_x layer satisfies the electronic structure requirements of the optical spacer.

Improved Efficiency with the Optical Spacer

Utilizing this TiO_x layer as the optical spacer, we fabricated donor/acceptor composite photovoltaic cells using the phase separated "bulk heterojunction" material comprising poly(3-hexylthiophene) (P3HT) as the electron donor and the fullerene derivative, [6,6]-phenyl-C_{61} butyric acid methyl ester (PCBM) as the acceptor. The device structure is shown in Fig. 6B

Fig. 8A compares the incident photon to current collection efficiency spectrum (IPCE) of devices fabricated with and without the TiO_x optical spacer. The IPCE is defined as the number of photo-generated charge carriers contributing to the photocurrent per incident photon. The conventional device (without the TiO_x layer) shows the typical spectral response of the P3HT:PCBM composites with a maximum

IPCE of ~60% at 500 nm, consistent with previous studies.. For the device with the TiO_x optical spacer, the results demonstrate substantial enhancement in the IPCE over the entire excitation spectral range; the maximum reaches almost 90% at 500 nm, corresponding to a 50% increase in IPCE.

We attribute this enhancement to increased absorption in the bulk heterojunction layer as a result of the TiO_x optical spacer; the increased photo-generation of charge carriers results from the spatial redistribution of the light intensity. In order to further clarify the role of the TiO_x layer, we measured the reflectance spectrum from a "device" with glass/P3HT:PCBM/TiO_x/Al geometry using a glass/P3HT:PCBM/Al "device" as the reference (the P3HT:PCBM composite film thickness, d, was about 100 nm in both). Note that the ITO/PEDOT layers were omitted to avoid any complication arising from the conducting layers. Since the two "devices" are identical except for TiO_x optical spacer layer, comparison of the reflectance yields information on the additional absorption, $\Delta\alpha(\omega)$, in the P3HT:PCBM composite film as a result of the spatial redistribution of the light intensity by the TiO_x layer (*32*)

$$\Delta\alpha(\omega) \approx - (1/2d)\ln[I'_{out}(\omega)/ I_{out}(\omega)] \qquad (1)$$

where $I'_{out}(\omega)$ is the intensity of the reflected light from the device with the optical spacer and $I_{out}(\omega)$ is the intensity of the reflected light from an identical device without the optical spacer. The data (Fig. 8B) demonstrate a clear increase in absorption over the entire spectrum. Moreover, since the spectral features of the P3HT:PCBM

absorption are evident in both spectra, the increased absorption arises from a better match of the spatial distribution of the light intensity to the position of the P3HT:PCBM composite film. We conclude that the higher absorption is caused by the TiO_x layer as an optical spacer as sketched in Fig. 6A. As a result, the TiO_x optical spacer increases the number of carriers per incident photon collected at the electrodes.

As shown in Fig. 9A, the enhancement in the device efficiency that results from the optical spacer can be directly observed in the current density vs voltage (J-V) characteristics under monochromatic illumination with 25 mW/cm^2 at 532 nm. The conventional device (without the TiO_x layer) shows typical photovoltaic response with device performance comparable to that reported in previous studies; the short circuit current (I_{sc}) is I_{sc} = 8.4 mA/cm^2, the open circuit voltage (V_{oc}) is V_{oc} = 0.60 V, and the fill factor (FF) is FF = 0.40. These values correspond to a power conversion efficiency (η_p) of η_e = 8.1%. For the device with the TiO_x layer, the results demonstrate substantially improved device performance; I_{sc} increases to I_{sc} = 11.8 mA/cm^2, the FF increases slightly to FF = 0.45, while V_{oc} remains at 0.60 V. The corresponding power conversion efficiency is η_e = 12.6%, which corresponds to ~50% increase in the device efficiency, consistent with the IPCE measurements.

Data from a cell with optical spacer obtained under AM1.5 illumination with irradiation intensity of 90 mW/cm^2 are shown in Fig. 9B. The device without the TiO_x layer again shows typical photovoltaic response with device performance comparable

to that reported in previous studies; I_{sc} = 10.1 mA/cm^2, V_{oc} = 0.56 V, FF = 0.55 and η_e = 3.5%. For the device with the TiO_x layer, the results demonstrate substantially improved device performance; I_{sc} = 11.1 mA/cm^2, V_{oc} = 0.61 V, FF = 0.66. The corresponding power conversion efficiency is η_e = 4.95 %, which corresponds to ~40% increase in the device efficiency.

Conclusion

In conclusion, polymer solar cells with power conversion efficiencies approaching 5% and remarkable thermal stability have been demonstrated after postproduction thermal annealing at 150^{o}C. We attribute the higher efficiency to thermally induced morphology modification, thermally induced crystallization and improved transport across the interface between the bulk heterojunction material and the Al electrode. The improved nanoscale morphology results in more efficient charge generation. The higher crystallinity and improved transport across the interface result in better charge collection at the electrodes with reduced series resistance and higher fill factor. We anticipate that by using the optical spacer architecture described here, one should be able to improve the performance to efficiencies in excess of 7%. Experiments are underway directed toward this goal.

Acknowledgement: This research was supported by Konarka Technologies (Lowell,

MA) and by the Air Force Office of Scientific Research, AFOSR, under FA9550-05-0139 and by AFOSR through the MURI Center ("Polymer Smart Skins", F49620-01-10364), Charles Lee, Program Officer. The research at Pusan National University (Busan, Korea) were supported by the Ministry of Information & Communication, Korea, under the Information Technology Research Center Support Program and by the National Program for Nanoscience and Technology of the Ministry of Science and Technology of Korea (M1-0214-00-0077).

REFERENCES

[1] G. Yu, J. Gao, J.C. Hummelen, F. Wudl, and A.J. Heeger, *Science* **1995***, 270***,** 1789.

[2] S.E. Shaheen, C.J. Brabec, N.S. Sariciftci, F. Padinger, T. Fromherz, and J.C. Hummelen, *Appl. Phys. Lett.* **2001,** *78***,** 841.

[3] J.M. Kroon, M.M. Wienk, W.J.H. Verhees, and J.C. Hummelen, *Thin Solid Films* **2002,** *403–404***,** 223.

[4] M. Svensson, F. Zhang, S.C. Veenstra, W.J.H. Verhees, J.C. Hummelen, J.M. Kroon, O. Ingana¨s, and M.R. Andersson, *Adv. Mater.* **2003***, 15***,** 988.

[5] M.M. Wienk, J.M. Kroon, W.J.H. Verhees, J. Knol, J.C. Hummelen, P.A. van Hall, and R.A.J. Janssen, *Angew. Chem. Int. Ed.* **2003,** *42***,** 3371.

[6] F. Padinger, R.S. Rittberger, and N.S. Sariciftci, *Adv. Funct. Mater.* **2003***, 13***,** 85.

[7] C.J. Brabec, A. Cravino, D. Meissner, N.S. Sariciftci, M.T. Rispens, L. Sanchez,

J.C. Hummelen, and T. Fromherz, *Thin Solid Films* **2002***,* 403–404**,** 368.

[8] H. Kim, S-H. Jin, H. Suh, and K. Lee *in Organic Photovoltaics IV,* (Eds: Z.H. Kafafi, and P.A. Lane, Proceedings of the SPIE, Vol. 5215), **SPIE, Bellingham, WA, 2004**, p. 111.

[9] A. L. Fahrenbrach and R.H. Bube*, Fundamentals of solar cells*, **Academic press, New York 1983**.

[10] H. C. Raus, *Solar cell array design handbook*, **Van Nostrand Reinhold Company, New York 1980**, p 56.

[11] P. Schilinsky, C. Waldauf, J. Hauch, and C.J. Brabec*, J. Appl. Phys.* **2004,** *95***,** 2816.

[12] I. Riedel and V. Dyakonov, *Phys. Status Solidi A* **2004***, 201*, 1332.

[13] D. Chirvase, J. Parisi, J.C. Hummelen and V. Dyakonov, *Nanotechnology* **2004,** *15*, 1317.

[14] N. Camaioni, G. Ridolfi, G. C.-Miceli, G. Possamai and M. Maggini, *Adv. Mater*. **2002**, *14*, 1735.

[15] J.J. Dittmer, R. Lazzaroni, P. Leclere, P. Moretti, M. Granstro¨m, K. Petritsch, E.A. Marseglia, R.H. Friend, J.L. Bredas, H. Rost, and A.B. Holmes, *Sol. Energy Mater. Sol. Cells* **2000,** *61***,** 53.

[16] J.J. Dittmer, E.A. Marseglia, and R.H. Friend, *Adv. Mater.* **2000***, 12***,** 1270.

[17] H. Hoppe, M. Niggemann, C. Winder, J. Kraut, R. Hiesgen, A. Hinsch, D.

Meissner, and N.S. Sariciftci, *Adv. Funct. Mater.* **2004**, *14*, 1005.

[18] C. J. Brabec, S. E. Shaheen, C. Winder, N. S. Sariciftci, P, Denk, *Appl. Phys. Lett.,* **2002**, *80*, 1288; P. Schilinsky, C. Waldauf, and C. J. Brabec, *Appl. Phys. Lett.* **2002**, *81*, 3885.

[19]Y. Kim, S. A. Choulis, J. Nelson, D. D. C. Bradley, S. Cook, J. R. Durrant, *Appl. Phys. Lett.* **2005**, *86*, 502.

[20] X. N. Yang, J. Loos, S. C. Veenstr, W. J. H. Verhees, M. M. Wienk, J. M. Kroon, M.A. J. Michels, R. A. J. Janssen, *Nano Lett*. **2005**, *5*, 579.

[21] J. M. Halls, K. Pichler, R.H. Friend, AS.C. Moratti, A.B. Holmes, *Appl. Phys. Lett*. **1996**, *68*, 3120.

[22] L.A.A. Pettersson, L.S. Roman, O. Ingannas, *J. Appl. Phys*. **1999**, *86*, 487.

[23] T.-A. Chen, X. Wu, R.D. Rieke, *J. Am. Chem. Soc*. **1995**, *117*,233.

[24] T.-W. Lee and O O. Park, *Adv. Mater.* **2000,** *12*, 801.

[25] P. Peumans, S. uchida and S.R. Forrest, *Nature*, **2003**, *425*, 158.

[26] J. Birgerson, M. Fahlman, P. Broms, W.R. Salaneck, *Synth. Met.* **1996**, *80*, 125.

[27] M. Logdlund, J.L. Bredas, *J. Chem. Phys.* **1994**, *101*, 4357.

[28] F.J. Esselink, G. Hadziioannou, *Synth. Met*. **1995**, *75*, 209.

[26] M. T. Rispens, A. Meetsma, R. Rittberger, C.J. Brabec, N.S. Sariciftci and J.C. Hummelen, *Chem. Commun*. **2003**, 2118-2118.

[27. L. A. A. Pettersson, L. S. Roman, O. Inganäs, *J. Appl. Phys*. **86**, 487 (1999).

[28]. T. Stübinger, W. Brütting, *J. Appl. Phys*. **90**, 3632 (2001).

[29]. H. Hänsel *et al.*, *Adv. Mater*. **15**, 2056 (2003).

[29]. H. J. Snaith, N. C. Greenham, R. H. Friend, *Adv. Mater.* **16**, 1640 (2004).

[30]. C. Melzer, E. J. Koop, V. D. Mihaletchi, P. W. M. Blom, *Adv. Funct. Mater.* **14**, 865 (2004).

[31]. Y. I. Kim *et al*., *J. Phys. Chem. B* **101**, 2491 (1997).

[32]. K. Lee, Y. Chang, J. Y. Kim, *Thin Solid Films* **423**, 131 (2003).

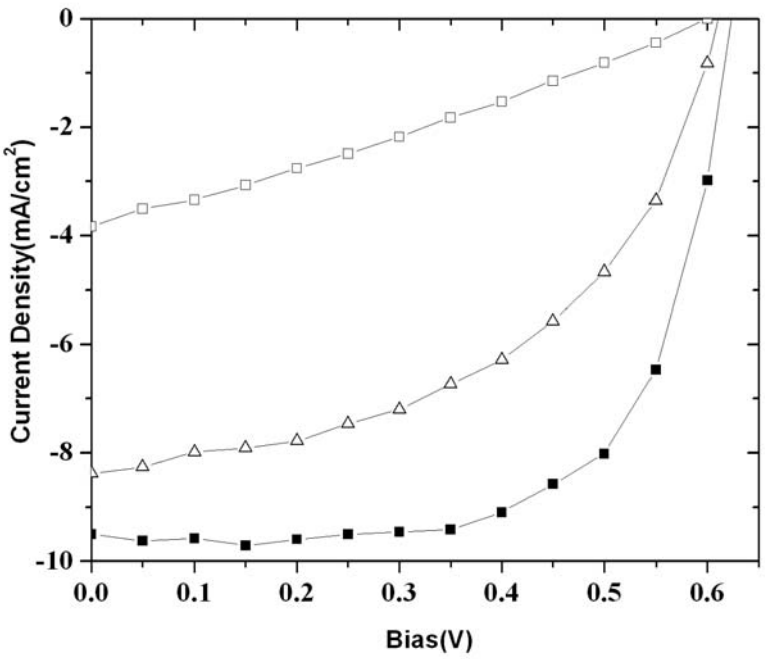

Figure 1. Current-voltage (I-V) curves obtained from P3HT:PCBM solar cells under AM 1.5 illumination at an irradiation intensity of 80mW/cm^2: Devices without thermal annealing(open squares), devices with postproduction heat treatment at 70^{0}C (open triangles) and devices with postproduction heat treatment at

150^0C(filled squares). All devices were annealed for 30 minutes. The device structure is the following: ITO/PEDOT/P3HT:PCBM/Al.

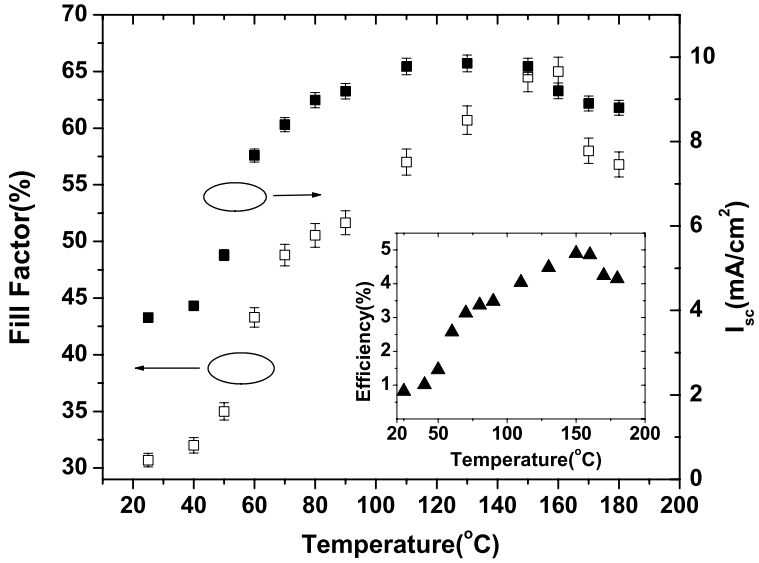

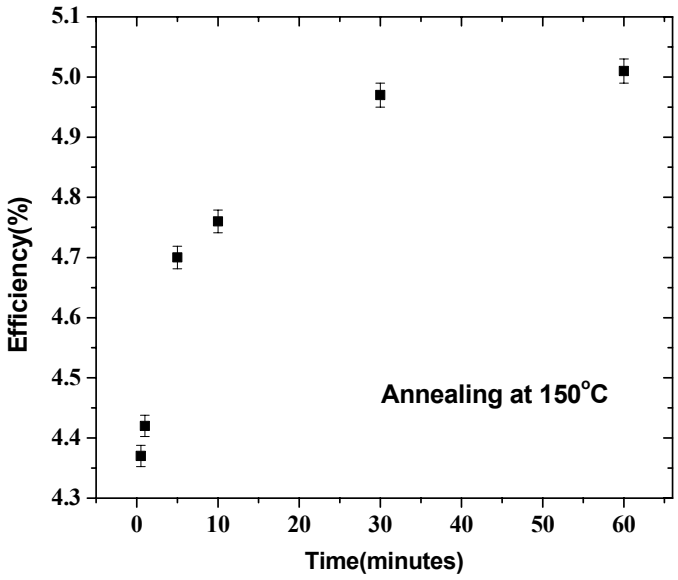

Figure 2.

a. Variation of fill factor (open squares) and short circuit current (filled squares) with annealing temperature (AM1.5, 80mW/cm^2). Inset shows the device efficiency vs annealing temperature. For these data, the annealing time was 15 minutes.
b. Evolution of device efficiency (filled squares) with thermal annealing time at 150^{0}C.

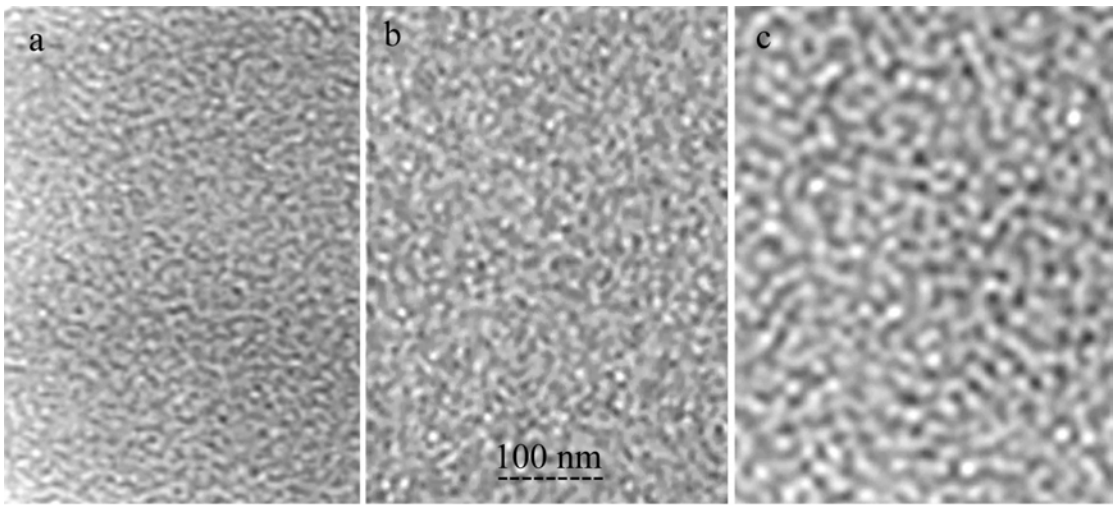

Figure 3. TEM images of P3HT:PCBM film bulk morphology before thermal annealing(a), after thermal annealing at 150^{o}C for 30 minutes(b) and after thermal annealing at 150^{o}C for 2 hours.

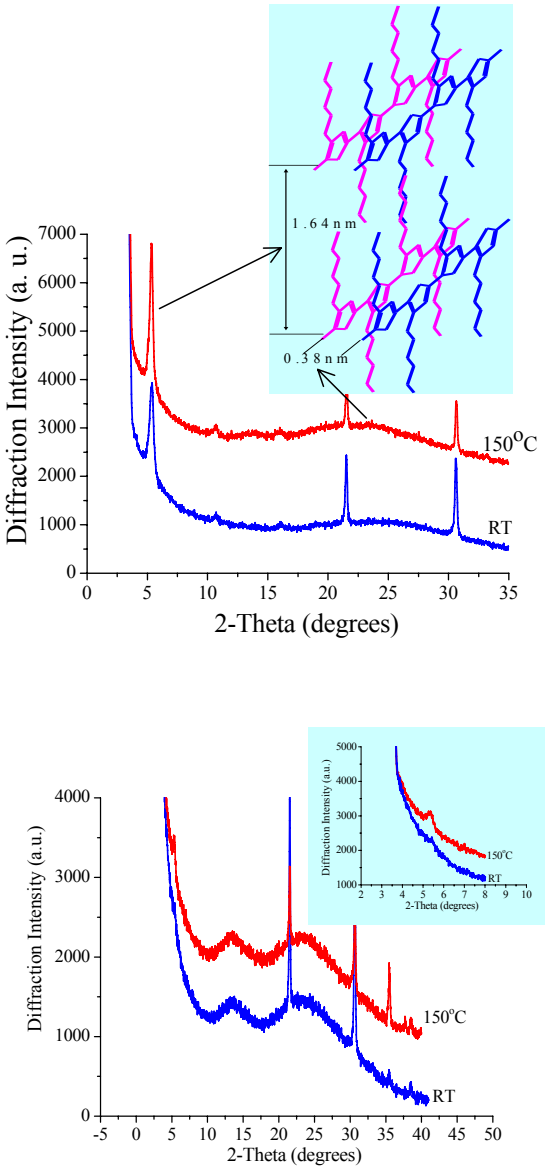

Figure 4

a. X-ray diffraction spectra of a P3HT:PCBM film drop-cast onto a PEDOT/ITO substrate with and without thermal annealing at 150°C for 30 minutes. The inset shows the P3HT crystal structure.

b. X-ray diffraction spectra obtained from completed solar cells (with Al electrode) before and after annealing at 150 °C for 30 minutes. The inset shows the region around $2\theta \approx 5$ degrees in greater detail. The peak at $2\theta \approx 13^{\circ}$ arises from the PEDOT layer and the peaks at $2\theta \approx 22^{0}$ and 31^{0} are from ITO.

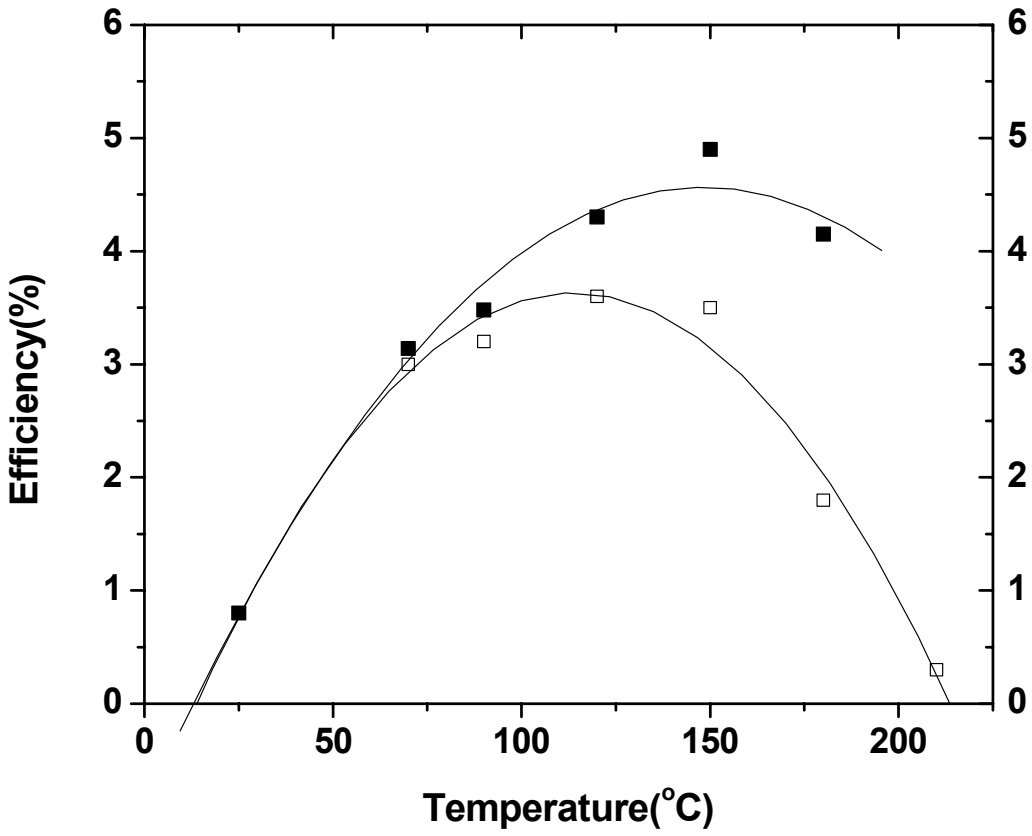

Figure 5. Solar cell efficiency vs annealing temperature for devices annealed at 150°C for 30 minutes before Al evaporation (open squares) and for devices annealed under the same conditions after Al deposition (filled squares).

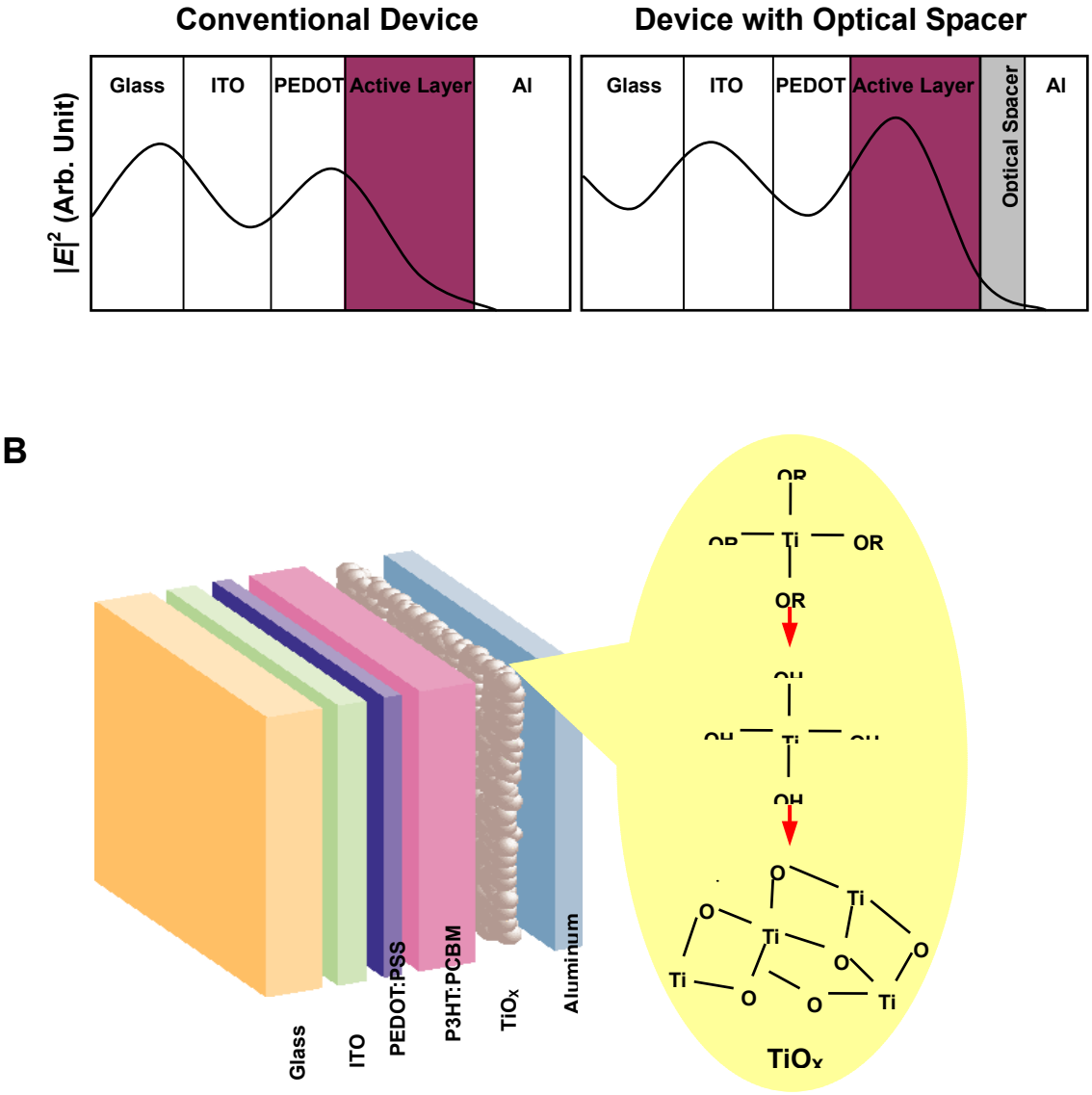

Fig. 6. (**A**) Schematic description of the optical spacer concept. Distribution of the squared optical electric field strength $|E|^2$ inside the devices with a structure of ITO/PEDOT/Active-Layer/Al (left) and ITO/PEDOT/Active-Layer/Optical Spacer/Al (right) is illustrated. The dot region in the left figure denotes the dead-zone as explained in the text. (**B**) Schematic illustration of the device structure. The TiO_x optical spacer layer is inserted between the active layer and an Al electrode. A brief flow chart is included showing the steps involved in the preparation of the TiO_x layer.

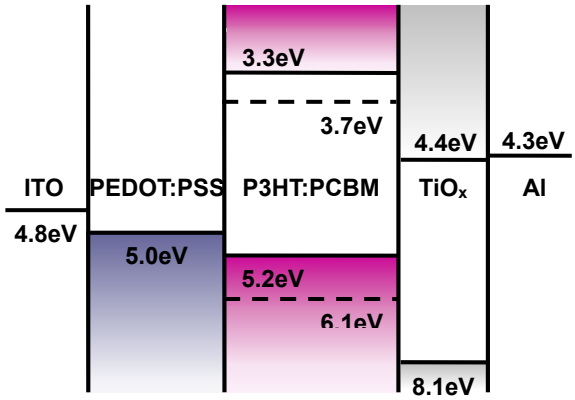

Fig. 7 Energy level of the single components of photovoltaic cell is also shown, which exhibits excellent band matching for cascading charge transfer in this system.

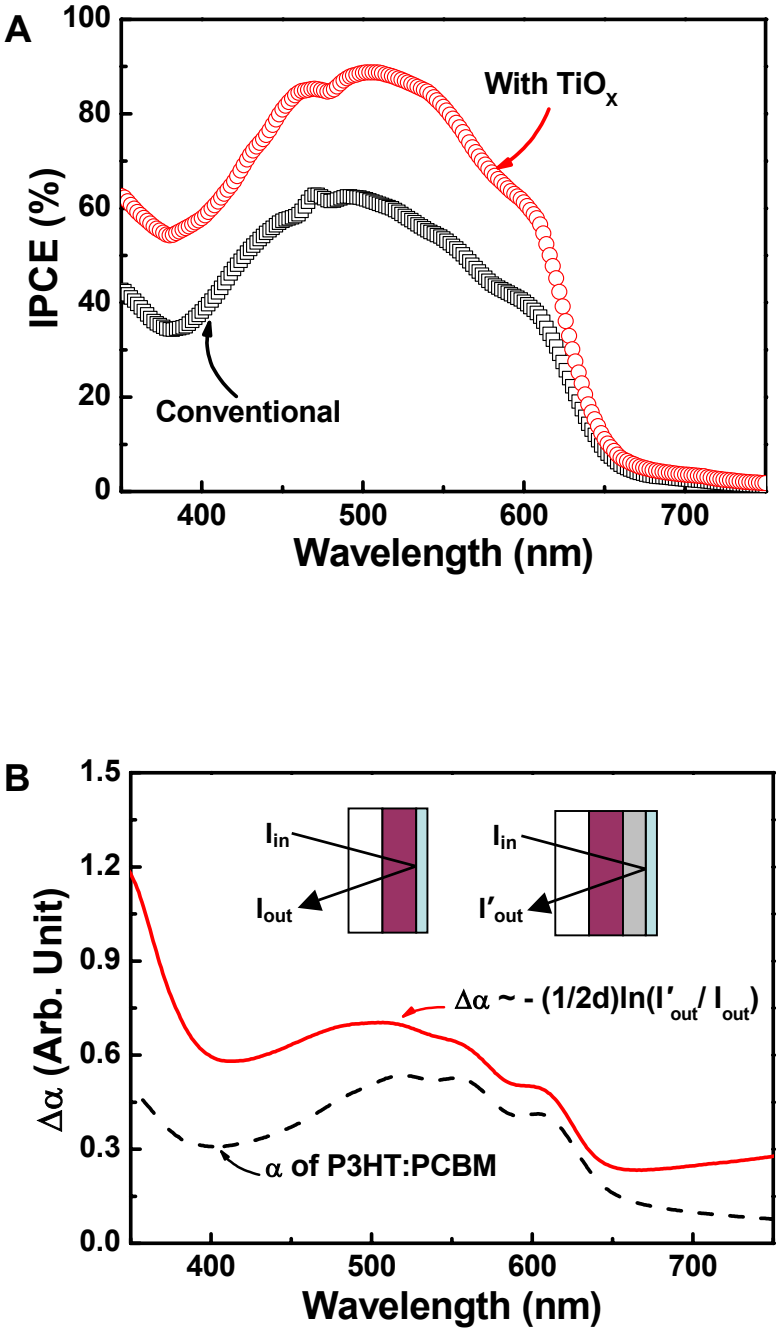

Fig. 8. (**A**) External quantum efficiency [EQE; same as the incident monochromatic photon to current collection efficiency (IPCE)] spectra for the two devices with and without TiO_x optical spacer layer. (**B**) The change in the absorption spectrum resulting from the addition of the optical spacer as given in Eq. (1) in the text.

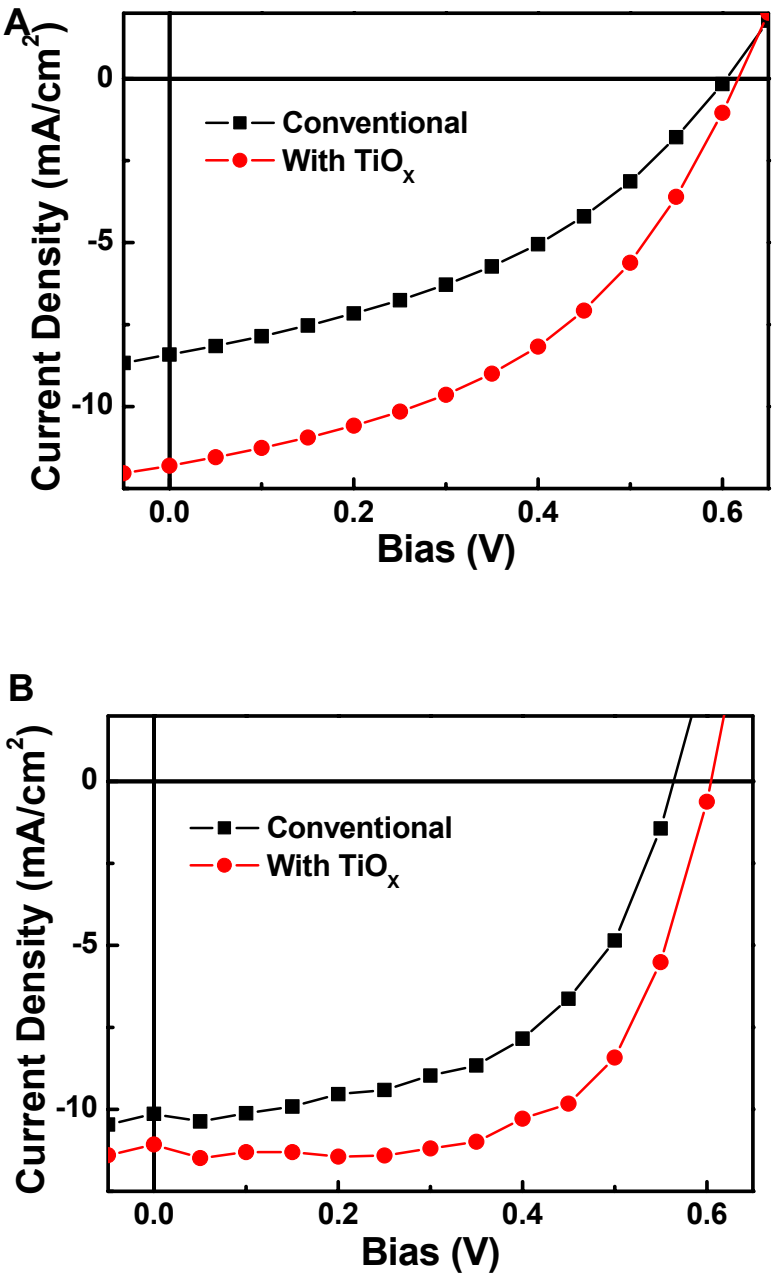

Fig. 9. (**A**) The current density-voltage (J-V) characteristics of polymer solar cells with (circle) and without (square) TiO_x optical spacer illuminated with 25 mW/cm^2 at 532 nm. (**B**) The J-V characteristics of polymer solar cells with (circle) and without (square) TiO_x optical spacer under AM1.5 illumination from a calibrated solar simulator with an intensity of 90 mW/cm^2.